Energy &
Environmental
Science

ROYAL SOCIETY OF CHEMISTRY

PAPER

View Article Online
View Journal | View Issue

Cite this: *Energy Environ. Sci.*, 2024, **17**, 3888

Ruthenium nanoparticles decorated with surface hydroxyl and borate species boost overall seawater splitting *via* increased hydrophilicity†

Le-Wei Shen,‡[a] Yong Wang,‡[a] Ling Shen,‡[a] Jiang-Bo Chen,‡[a] Yu Liu,[a] Ming-Xia Hu,[a] Wen-Ying Zhao,[a] Kang-Yi Xiong,[a] Si-Ming Wu,[a] Yi Lu,[a] Jie Ying,[c] Maria Magdalena Titirici,[d] Christoph Janiak,[e] Ge Tian*[a] and Xiao-Yu Yang*[ab]

Received 29th February 2024,
Accepted 29th April 2024

DOI: 10.1039/d4ee00950a

rsc.li/ees

The use of seawater electrolysis for hydrogen production faces several serious challenges, including the rapid deactivation of electrocatalysts through chloride anion (Cl^-) induced corrosion. We have demonstrated that Ru nanoparticles possessing an abundance of surface hydroxyl groups along with borate species (Ru–BO_x–OH) exhibit high activity and stability as electrocatalysts for seawater splitting. The optimal electrocatalyst (Ru–BO_x–OH-300) uncovered in this study displays an extremely high catalytic performance for both the hydrogen (HER) and oxygen (OER) evolution reactions in alkaline seawater (HER, 22 mV and OER, 235 mV at 10 mA cm^{-2}), as well as a low cell voltage (1.47 V) and ultra-long-term stability (1000 hours at 10, 50 and 100 mA cm^{-2}) for overall seawater splitting. Furthermore, the Ru–BO_x–OH-300-based anion-exchange membrane seawater electrolyzer requires only 1.73 or 1.95 V to reach a current density of 500 or 1000 mA cm^{-2}, respectively, and exhibits excellent stability for 400 hours without obvious decay. The results of the experiments and theoretical calculations reveal that the high water affinity of Ru–BO_x–OH-300 caused by the presence of hydroxyl and borate species on the metallic Ru surface is responsible for the superb electrocatalytic performance and that the borate species are the source of Cl^- corrosion resistance. These findings provide new perspectives for the design of high-performance electrocatalysts for seawater splitting.

Broader context

To achieve the practical usage of renewable ocean energy, electrolysis of seawater, one of the most important issues, should be fulfilled by developing efficient and stable electrocatalysts. Unfortunately, the presence of chloride (Cl^-) in seawater will rapidly inactivate the electrocatalysts, and it is necessary to develop effective catalysts that can resist seawater corrosion. Ruthenium (Ru)-based electrocatalysts exhibit favorable performances in the electrochemical hydrogen evolution reaction (HER) and oxygen evolution reaction (OER). However, the performance degradation of Ru caused by the formation of water-soluble Ru oxides during the OER is a bottleneck. To resolve these issues, introducing surface reactive species is an effective strategy because they can regulate the electrons around Ru and alleviate further oxidation of Ru during the OER. However, the introduction of surface-reactive species on Ru-based electrocatalysts by a simple and effective method has hardly been developed. Herein, we demonstrate that surface hydroxyl and borate species on metallic Ru nanoparticles significantly promote the activity and stability for overall seawater splitting. The mild synthesis method for Ru-based electrocatalysts described in this work would be greatly useful for the development of active and stable catalysts as well as for avoiding Cl^- corrosion.

---

[a] *State Key Laboratory of Advanced Technology for Materials Synthesis and Processing, and International School of Materials Science and Engineering, and School of Materials Science and Engineering, and Shenzhen Research Institute, and Laoshan Laboratory, Wuhan University of Technology, Wuhan, Hubei, 430070, China. E-mail: xyyang@whut.edu.cn, tiange@whut.edu.cn*

[b] *National Energy Key Laboratory for New Hydrogen-Ammonia Energy Technologies Foshan Xianhu Laboratory, Foshan 528200, P.R. China*

[c] *School of Chemical Engineering and Technology, Sun Yat-sen University, Zhuhai 519082, China*

[d] *Department of Chemical Engineering, Imperial College London, London SW7 2AZ, England, UK*

[e] *Institut für Anorganische Chemie und Strukturchemie, Heinrich-Heine-Universität Düsseldorf, Düsseldorf 40204, Germany*

† Electronic supplementary information (ESI) available. See DOI: https://doi.org/10.1039/d4ee00950a

‡ These authors contributed equally to this study.

Introduction

Continuity and stability are major bottlenecks hindering the development of renewable ocean energy approaches.[1,2] Seawater electrolysis technology is considered promising for utilizing this renewable resource for the continuous generation of energy in the form of storable and transportable hydrogen (H_2). Indirect seawater electrolysis (ISE, *e.g.*, seawater reverse osmosis with a pure water electrolyzer system) has been found to be more effective in terms of cost and hydrogen production than direct seawater electrolysis (DSE) due to the mature desalination and electrolysis technologies.[3,4] However, with the rapid development of electrocatalysts, electrolyzer design and electrolysis technology, as well as the low electricity cost from coastal solar and offshore wind energy, the cost of DSE will be significantly reduced.[5,6] It has been estimated that the cost proportion of the desalination process will reach $\geq 7\%$ for an alkaline electrolyzer system, which cannot be ignored in the ISE.[7] Moreover, reverse osmosis seawater desalination is aimed at living needs in some arid areas, as ISE with reverse osmosis is not suitable for sustainable development in these areas.[8,9] As a result, it is necessary to develop DSE for large-scale hydrogen production.

The major challenge of DSE is the rapid deactivation of electrocatalysts caused by chloride (Cl^-)-induced corrosion at the anode.[10,11] Ruthenium (Ru) is an ideal electrocatalyst for the hydrogen (HER) and oxygen (OER) evolution reactions because of its attractive electrocatalytic performance and remarkable stability in seawater under low applied potentials (<0.4 V, *vs.* RHE).[12,13] However, Ru electrocatalysts are readily overoxidized to form water-soluble Ru oxides at OER operating potentials (>1.4 V, *vs.* RHE), and Cl^- coordination accelerates the leaching process of Ru.[14–16] Therefore, great interest exists in developing approaches to improve the electrocatalytic activity and stability of Ru-based electrocatalysts for seawater splitting.[17,18]

Surface hydroxyl species (–OH) have high water affinities, which enhance the efficiency of electrocatalytic water splitting.[19–21] For example, transition-metal hydroxides and reconstructed hydroxides formed by many metals/oxides are considered to be the actual electrocatalytic sites for water splitting.[22–24] Moreover, owing to their negative charge and water affinity, hydroxyl species can prevent Cl^- adsorption and consequent electrocatalyst corrosion.[25–27] Unfortunately, the observation that Ru–OH formation occurs only on the surfaces of Ru oxides suggests that the introduction of stable hydroxyl on the metal Ru cannot be performed by using well-known methods such as steam-thermal treatment and alkaline hydro-/solvo-thermal synthesis.[28,29] From another perspective, it is known that boron (B) can be easily incorporated into metals, and that metal boron doping is an effective method to enhance chemical and structural stability.[30,31] Also, B can couple with hydroxyl groups on metal surfaces to form surface-boronated hydroxyl around the metal nanostructures.[32,33] However, it should be noted that conventional boriding protocols involve the use of high temperatures (>800 °C) at which hydroxyl groups are readily lost.[34,35]

In the effort described below, we devised a room-temperature reduction and low-temperature calcination (300 °C) approach to prepare Ru nanoparticles, denoted as Ru–BO_x–OH-300, which contain enriched hydroxyl and borate species on the surface. The formation of surface hydroxyls in this process and their effects on water affinity have been verified experimentally. Benefiting from the high hydrophilicity of the surface hydroxyl groups, Ru–BO_x–OH-300 serves as an excellent electrocatalyst for alkaline seawater splitting. Experimental and density functional theory (DFT) results indicate that the surface hydroxyl and borate species regulate the Ru catalytic sites in Ru–BO_x–OH-300, which promotes H_2O dissociation and thereby reduces the activation energy for the electrolytic splitting of water to form O_2 and H_2. Moreover, the borate species increase the resistance of the electrocatalyst to Cl^- adsorption and hence improve its stability in seawater.

Results and discussion

Materials synthesis and characterization

A schematic representation of the method used to construct Ru–BO_x–OH-300 nanoparticles is shown in Fig. 1a. In this route, the precursor to the catalyst was generated by the reduction of $RuCl_3$ using an alkaline $NaBH_4$ solution[36] and then subjected to calcination under an argon atmosphere[37] (see the ESI† with Experimental procedures for details). The formed electrocatalysts are designated as Ru–BO_x–OH-*T*, where *T* is the calcination temperature. We also showed that the B content of the surface of the electrocatalysts could be regulated by controlling the pH of the $NaBH_4$ solution and the calcination temperature (see Fig. S1 and S2, Table S1, and a detailed description, ESI†).[37] The results of XPS (Fig. S2, ESI†) and ICP-AES (Table S1, ESI†) analysis indicate that the B content of the surface is increased upon calcination, owing to migration of relatively light B atoms from the bulk to the surface during annealing.[38]

A plot of the thermogravimetric analysis with differential scanning calorimetry (TG-DSC) data for the as-prepared Ru–BO_x–OH precursor contains two exothermic peaks at *ca.* 230 and *ca.* 330 °C (Fig. S3, ESI†). The analysis of the X-ray diffraction (XRD) patterns (Fig. 1b) of the as-prepared Ru–BO_x–OH and composites generated by annealing at temperatures between 200–350 °C shows that the intensities of the signals for hexagonal closest-packed (hcp) metallic Ru increase as the temperature increases between 200–300 °C, and that the rutile ruthenium oxide (RuO_2) phase forms at temperatures *ca.* 350 °C. In detail, the peaks corresponding to Ru–BO_x–OH-200 and Ru–BO_x–OH-300 at 38° for the Ru (100) plane and 44° for the Ru (101) plane (ICDD no. 06-0663) are present in the diffraction profiles and their intensities are greater than that of the single broad diffraction peak at 42° for Ru–BO_x–OH. The calcination-promoted shift of the broad peak in the pattern of Ru–BO_x–OH-*T* from 42° to 44° suggests that a reduction of interplanar spacing takes place, which is likely caused by crystal reorganization bringing B to the surface. This suggestion is in good agreement with the increase of the surface B content, as indicated by the XPS and ICP-AES results (Fig. S2 and Table S1, ESI†). After annealing at higher temperatures

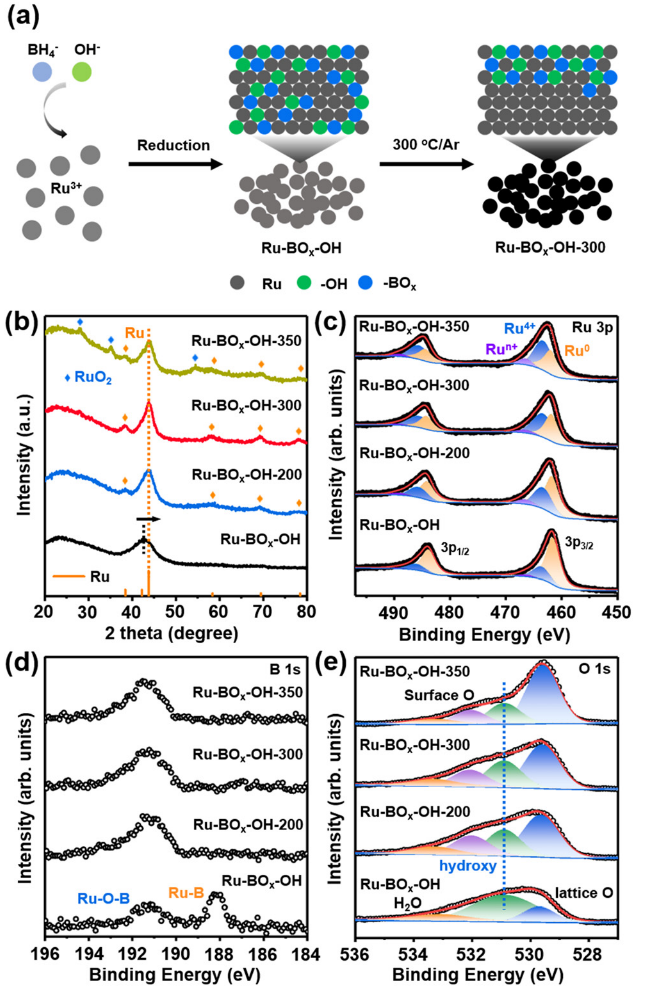

Fig. 1 (a) Schematic of the formation of Ru–BO$_x$–OH-300 nanoparticles. (b) XRD patterns of Ru–BO$_x$–OH, Ru–BO$_x$–OH-200, Ru–BO$_x$–OH-300 and Ru–BO$_x$–OH-350; (c) Ru 3p, (d) B 1s and (e) O 1s XPS spectra of Ru–BO$_x$–OH, Ru–BO$_x$–OH-200, Ru–BO$_x$–OH-300 and Ru–BO$_x$–OH-350.

(≥350 °C), the peaks of RuO_2 (ICDD no. 43-1027) are present in the diffraction profile. The formed RuO_2 originates from the amorphous oxidized species generated during the preparation process.[39] In summary, the combined observations show that a crystalline transformation to metallic Ru takes place during calcination at *ca.* 230 °C and that an oxidative phase transformation to RuO_2 occurs at *ca.* 330 °C.

X-ray photoelectron spectroscopy (XPS) was performed to determine the surface chemical states of Ru–BO$_x$–OH-*T*. The deconvoluted Ru 3p spectra (Fig. 1c) contain Ru $3p_{3/2}$ peaks at *ca.* 461.9 eV, which are ascribed to metallic Ru^0, along with peaks at higher binding energies (*ca.* 463.6 eV) attributed to Ru^{4+}.[40] The $Ru^0 : Ru^{4+}$ ratios are 2.3 for Ru–BO$_x$–OH, 1.7 for Ru–BO$_x$–OH-200, 0.9 for Ru–BO$_x$–OH-300 and 0.7 for Ru–BO$_x$–OH-350. This trend reflects the increase in the degree of surface ruthenium oxidation that occurs at increasing calcination temperatures, which is consistent with the XRD results. The B 1s spectrum (Fig. 1d) of Ru–BO$_x$–OH contains two distinct peaks at 188.2 and 191.2 eV. The former is assigned to B bound to Ru and the latter to the Ru–O–B bond in metal borates or B–O bound in B_2O_3.[41,42] Upon annealing, the peak at *ca.* 188.2 eV disappears, leaving behind only the signals attributed to Ru–O–B or B–O bonds. The O 1s spectra (Fig. 1e) peaks at *ca.* 530.9 eV are associated with the surface hydroxyls in Ru–BO$_x$–OH arising in the alkaline reaction medium and the intensities of these peaks decrease with increasing annealing temperature. The peak ascribed to the lattice oxygen at *ca.* 529.6 eV enhances with the increasing annealing temperature, which is due to the formation of RuO_2 at higher temperatures.[41]

The presence of hydroxyl groups in the Ru-based materials can be further characterized using Fourier transform infrared (FT-IR) and Raman spectroscopy after vacuum drying. For this purpose, metallic Ru nanoparticles Ru–O$_x$ and Ru–O$_x$-300 (see ESI† with Experimental Procedures for details, Fig. S4) that do not contain B serve as a control. Inspection of the FT-IR and Raman spectra confirms that the incorporation of borate species benefits the formation of hydroxyl species on the Ru nanoparticle surfaces and that, compared to those in Ru–O$_x$-300, the hydroxyl species in Ru–BO$_x$–OH-300 are stable during annealing (see Fig. S5 and S6 and a detailed description, ESI†).[43,44] The rich and stable hydroxyl species cause Ru–BO$_x$–OH-300 to have higher hydrophilicity than Ru–O$_x$-300 (Fig. S7, ESI†), which should promote a better electrocatalytic performance and the avoidance of Cl^--promoted corrosion during seawater electrolysis.[27,28]

Scanning electron microscopy (SEM) images show that Ru–BO$_x$–OH-*T* consist of interconnected nanoparticles with sizes of 10–40 nm (Fig. S8, ESI†). Owing to its optimized HER and OER performance (see below), Ru–BO$_x$–OH-300 was subjected to detailed transmission electron microscopy (TEM) studies (see Fig. S9 and a detailed description, ESI†). TEM images of this substance indicate that the individual nanoparticles are composed of much smaller particles with an average size of *ca.* 5 ± 1 nm (Fig. 2a and Fig. S10, ESI†), and a specific surface area of 60 $m^2\ g^{-1}$ (Fig. S11, ESI†). The inspection of the selected area (Fig. 2a) electron diffraction (SAED) patterns displayed in Fig. 2b indicates that diffraction rings indexed to the (002), (101), (102), (110) and (112) planes of the hcp Ru metal are present. The high-resolution TEM (HRTEM) image in Fig. 2c suggests that the particles have lattice spacings of 0.20 nm and 0.21 nm, which match the respective (101) and (002) planes of the Ru metal. The diffraction pattern (Fig. 2d), derived from the fast Fourier transformation (FFT) of the region I in Fig. 2c, contains signals indexed to the (101) and (002) planes of the Ru metal. The crystal lattice fusion of the Ru nanoparticles in Ru–BO$_x$–OH-300 can be ascertained by inspecting the inverse FFT image (Fig. 2e) of the diffraction pattern in Fig. 2d. Finally, energy-dispersive X-ray (EDX) spectroscopy analysis indicates that Ru, B and O are uniformly distributed in Ru–BO$_x$–OH-300 nanoparticles (Fig. 2f).

Electrocatalytic performance of the HER and OER

The electrocatalytic HER and OER performance of Ru–BO$_x$–OH-300, along with that of non-boron-containing Ru–O$_x$-300 and other materials, were evaluated using a standard three-

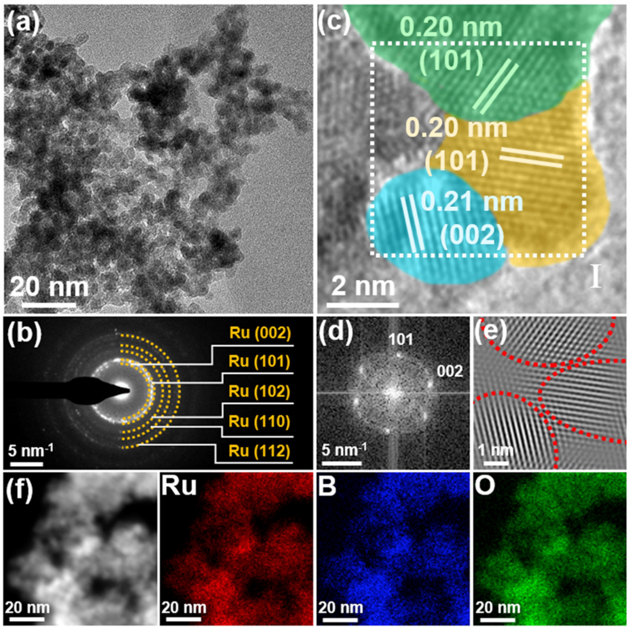

Fig. 2 (a) TEM image of Ru–BO$_x$–OH-300. (b) Corresponding SAED pattern in Fig. 2a. (c) HRTEM image of Ru–BO$_x$–OH-300. (d) Inverse FFT image of the diffraction pattern of the region I in Fig. 2c. (e) Diffraction pattern in Fig. 2d from FFT. (f) HAADF-STEM image of Ru–BO$_x$–OH-300 and EDX mapping images of Ru, B and O.

electrode system. The results show that Ru–BO$_x$–OH-300 has excellent HER and OER performance and durability in 0.5 mol L^{-1} H_2SO_4 and 1.0 mol L^{-1} KOH (see Fig. S12 and a detailed description, ESI†). These electrocatalysts were further evaluated in alkaline seawater (1.0 mol L^{-1} KOH + 3.5% wt. NaCl). The plots in Fig. 3a and b demonstrate that Ru–BO$_x$–OH-300 has an HER activity of 22 mV at a current density of 10 mA cm^{-2} (denoted as n_{10}), which is superior to those of commercial Pt/C (n_{10} = 32 mV) and Ru–O$_x$-300 (n_{10} = 68 mV). It is noteworthy that the HER activity of Ru–BO$_x$–OH-300 is comparable to that of recently described Ru-based electrocatalysts (Table S2, ESI†). Moreover, the Tafel slope of Ru–BO$_x$–OH-300 (16.9 mV dec^{-1}) arising from the plot shown in Fig. 3c is smaller than that of Ru–O$_x$-300 (53.8 mV dec^{-1}), suggesting an improved HER kinetics of Ru–BO$_x$–OH-300 (Fig. 3c). Also, the electrochemical double-layer capacitance (C_{dl}) of Ru–BO$_x$–OH-300 (32.2 mF cm^{-2}) is greater than that of Ru–O$_x$-300 (9.0 mF cm^{-2}), indicating the increased number of surface catalytic sites of Ru–BO$_x$–OH-300 (Fig. S13, ESI†). Nyquist plots show that Ru–BO$_x$–OH-300 has a smaller HER resistance than Ru–O$_x$-300 (Fig. S14, ESI†). These results indicate that the introduction of hydroxyl and borate species significantly improves the HER performance of Ru nanoparticles.

As shown in Fig. 3d, the n_{10} values of Ru–BO$_x$–OH-300, Ru–O$_x$-300 and Pt/C increase by 10, 22 and 192 mV, respectively, after 20 hours in a chronoamperometric test, and the negligible activity decay of Ru–BO$_x$–OH-300 at 100 mA cm^{-2} within 25 hours is detected (Fig. S15, ESI†), which indicates that Ru–BO$_x$–OH-300 has excellent stability for the HER. Additionally, the results of inductively coupled plasma-atomic emission spectroscopy (ICP-AES) show that the amount of dissolved Ru after 20 hours of the HER is low for Ru–BO$_x$–OH-300 (3%) and Ru–O$_x$-300 (4%), indicating that both electrocatalysts have high stability (Fig. 3e and Table S3 and S4, ESI†). SEM and TEM images after the HER stability test for 20 hours confirm that the morphology and structure of the Ru–BO$_x$–OH-300 nanoparticles are fully retained (Fig. S16 and S17, ESI†). Also, the XRD pattern of Ru–BO$_x$–OH-300 after 20 hours of the HER (Fig. S18, ESI†) still contains diffraction peaks ascribed to hcp metallic Ru. In addition, the XPS spectra of Ru–BO$_x$–OH-300 after the HER stability test suggest that peaks associated with Ru^{4+} (463.6 eV), Ru^{0} (462.0 eV), borate species (191.4 eV) and surface hydroxyl groups (530.9 eV) are still present (Fig. S19, ESI†). Raman spectroscopy further verifies that the surface hydroxyl groups of Ru–BO$_x$–OH-300 are retained after the HER stability test (Fig. S20, ESI†). The above results indicate that the Ru–BO$_x$–OH-300 catalyst after HER evaluation consists of mainly Ru nanoparticles with surface structures of some Ru oxide, borate species, and hydroxyl groups, and it shows outstanding HER activity as well as superior stability.

The OER performances of these materials in alkaline seawater were also assessed. As shown in Fig. 3f and g, the OER activity of Ru–BO$_x$–OH-300 (n_{10} = 235 mV) is much higher than that of Ru–O$_x$-300 (n_{10} = 349 mV) and RuO_2 (n_{10} = 371 mV), as well as that of recently reported Ru-based OER catalysts (Table S5, ESI†). The Tafel slope of Ru–BO$_x$–OH-300 (48.1 mV dec^{-1}, Fig. 3h) is lower than that of Ru–O$_x$-300 (52.7 mV dec^{-1}) and RuO_2 (55.8 mV dec^{-1}). Analysis of C_{dl} plots (Fig. S21, ESI†) indicates that Ru–BO$_x$–OH-300 (22.7 mF cm^{-2}) possesses more exposed active sites than Ru–O$_x$-300 (8.7 mF cm^{-2}) and RuO_2 (4.2 mF cm^{-2}). Moreover, the reaction resistance of Ru–BO$_x$–OH-300 obtained from Nyquist plots is smaller than that of Ru–O$_x$-300, indicating that the hydroxyl and borate species enhance electron transport in the OER (Fig. S22, ESI†). Importantly, after 20 hours of chronopotentiometry measurements (Fig. 3i), the n_{10} value of Ru–BO$_x$–OH-300 increases by only 36 mV, while the activities of Ru–O$_x$-300 and RuO_2 are lost after 13 and 6.5 hours, respectively. Moreover, no dramatic increase of the OER overpotential was observed for Ru–BO$_x$–OH-300 at 100 mA cm^{-2} during 25 hours (Fig. S23, ESI†). These findings indicate that the OER stability of Ru nanocomposites is improved by the presence of the hydroxyl and borate species. The ICP-AES results show that (Fig. 3j, Table S3 and S6, ESI†) although 9% of Ru from Ru–BO$_x$–OH-300 becomes dissolved in alkaline seawater after a 20 hour OER test, the dissolution rate reduces to a value lower than 0.1 mg L^{-1} h^{-1} after 10 hours, while 42% of Ru was dissolved for Ru–O$_x$-300 after 12 hours and the dissolution rate was high (0.6 mg L^{-1} h^{-1}). The results show that Ru–BO$_x$–OH-300 is highly resistant to anodic corrosion during the OER. The faradaic efficiency of the OER promoted by Ru–BO$_x$–OH-300 is *ca.* 98.1%, indicating that O_2 is almost the sole product generated at the anode (see Fig. S24, Table S7 and a detailed description, ESI†).

SEM images confirm that the morphology of Ru–BO$_x$–OH-300 is retained after OER testing while the Ru–O$_x$-300 nanoparticles agglomerated during this process (Fig. S25, ESI†).

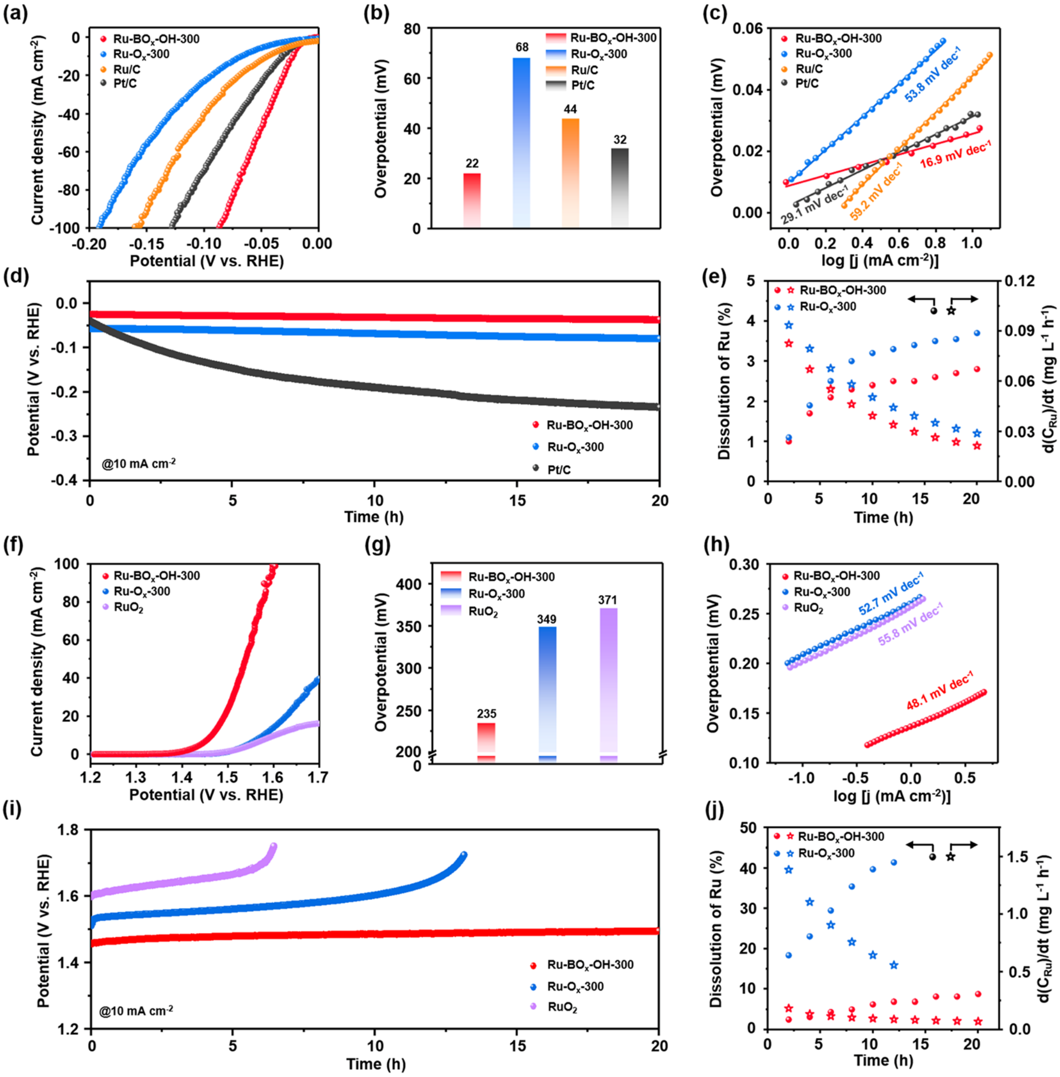

Fig. 3 HER and OER performance of Ru–BO$_x$–OH-300, Ru–O$_x$-300, Pt/C, Ru/C and RuO$_2$ in alkaline seawater. (a) Polarization curves for the HER. (b) Comparison of HER overpotentials at 10 mA cm^{-2}. (c) Tafel plots for the HER. (d) Chronoamperometric tests at a current density of 10 mA cm^{-2}. (e) ICP analysis of the Ru concentration and dissolution rate of Ru in an electrolyte for Ru–BO$_x$–OH-300 and Ru–O$_x$-300 during 20 hours of the HER chronoamperometric test at 10 mA cm^{-2}. (f) Polarization curves for OER. (g) Comparison of the OER overpotential at 10 mA cm^{-2}. (h) Tafel plots for the OER. (i) Chronoamperometric test at a current density of 10 mA cm^{-2}. (j) ICP analysis of the Ru concentration and dissolution rate of Ru in the electrolyte for Ru–BO$_x$–OH-300 and Ru–O$_x$-300 during 20 hours of the OER chronoamperometric test at 10 mA cm^{-2}.

The TEM images indicated that the crystallinity of Ru–BO$_x$–OH-300 is weakened, and RuO$_2$ species are detected in the sample (Fig. S26, ESI†). Likewise, the analysis of XRD patterns shows that the diffraction peaks characteristic of Ru metal for Ru–BO$_x$–OH-300 are weakened while they disappear completely for Ru–O$_x$-300. Rutile RuO$_2$ phases are formed for both Ru–BO$_x$–OH-300 and Ru–O$_x$-300 after the OER stability tests (Fig. S27, ESI†). XPS was conducted to further determine the surface structure of the catalysts. In the XPS spectra (Fig. S28, ESI†), the oxidation state of Ru for Ru–BO$_x$–OH-300 increased after the OER test, and the peaks of the borate species and surface hydroxyl groups are still observed. In contrast, the Ru 3p XPS signal for Ru–O$_x$-300 is significantly decreased due to severe anodic corrosion. Raman spectroscopy further confirmed that the intensities of RuO$_2$ and Ru–OH for Ru–BO$_x$–OH-300 are enhanced after OER measurements (Fig. S29, ESI†). The above results indicate that RuO$_2$ mixed with borate and hydroxyl groups is formed during the OER in the Ru–BO$_x$–OH-300 nanoparticles, while the borate species and hydroxyl groups can prevent the excessive oxidation and dissolution of Ru nanoparticles, finally enhancing both the catalytic activity and the stability of Ru–BO$_x$–OH-300 during the OER.

Effect of B sites and adsorbed hydroxyl formation

To further verify that the presence of B sites is responsible for the catalytic activity enhancement, a poisoning experiment using a low concentration of potassium thiocyanate (KSCN) was carried out (see ESI† with Experimental Procedures for details).[45–48] We expected that preferential binding of the Lewis basic SCN$^-$ to Lewis acid B sites would lead to poisoning and reduced electrocatalytic performance.[37] As shown in Fig. 4a, the current density of the HER catalyzed by Ru–BO_x–OH-300 remains nearly unchanged for 400 s in the absence of KSCN, while it decreases significantly after the addition of KSCN (by *ca.* 3.3 mA cm^{-2} from 400 to 800 seconds and by *ca.* 2.3 mA cm^{-2} from 800 to 1200 seconds). Similarly, the OER performance of Ru–BO_x–OH-300 is also reduced by the addition of KSCN (current density is decreased by *ca.* 3.1 and *ca.* 3.6 mA cm^{-2} after the addition of KSCN) (Fig. 4b). In contrast, the HER and OER activities of Ru–O_x-300 are barely affected by the addition of KSCN. Specifically, the current density of the HER-catalyzed by Ru–O_x-300 slightly decreases by *ca.* 0.5 and *ca.* 0.4 mA cm^{-2} after the addition of KSCN (Fig. 4c). For the OER promoted by Ru–O_x-300 (Fig. 4d), the current density decreases steadily, which is attributed to the poor OER stability of the catalyst. To further verify the role of borate species, the HER and OER performance of Ru–BO_x–OH-300 was evaluated at different concentrations of BO_3^{3-} ions. As shown in Fig. 4e and f, the HER and OER performance of Ru–BO_x–OH-300 was enhanced apparently in the electrolyte with a high concentration of BO_3^{3-} ($\geq$0.25 mmol L^{-1}). Considering that the pH of the electrolyte was controlled to be the same (see ESI† with Experimental Procedures for details), the HER and OER performance enhancement could be attributed to the surface ruthenium and borate coordination.[49,50] The results indicate that the catalytic HER and OER performance of Ru–BO_x–OH-300 is significantly diminished by poisoning the B sites and increased with the addition of BO_3^{3-} ions, confirming the proposal that borate species are responsible for the improved electrocatalytic properties.

CO-stripping experiments were conducted to compare the difficulty of forming adsorbed hydroxyl (OH*) on the surface of Ru-based electrocatalysts, which is also the first step reaction in the OER process.[51] In this experiment, a monolayer of CO pre-adsorbed on the surface of the electrocatalyst is electrochemically oxidized (referred to as CO stripping). It is usually considered that OH* facilitates CO stripping and reduces the oxidation potential of CO. Thus, the propensity for OH* formation on the surface of the catalyst is reflected in a reduction in the potential of the CO peak stripping.[52,53] The results arising from these experiments show that the CO stripping peak on Ru–BO_x–OH-300 (0.59 V) is shifted to a lower potential compared to those of Ru–BO_x–OH (0.60 V) and Ru–O_x-300 (0.70 V), indicating that OH* can be easily formed on the surface of Ru–BO_x–OH-300 (Fig. 4g).[52]

Electrocatalytic overall seawater splitting

Overall, seawater splitting determinations were made on the Ru-based nanocomposites used as both anodic and cathodic electrocatalysts. As shown in Fig. 5a and b, the Ru–BO_x–OH-300‖Ru–BO_x–OH-300 based device has excellent activity with a voltage of 1.47 V, delivering a current density of 10 mA cm^{-2}. This value is significantly lower than those of devices comprised of Ru–O_x-300‖Ru–O_x-300 (1.57 V) and Pt/C‖RuO_2 (1.52 V). To ascertain whether the chlorine evolution reaction (CER) at the anode occurred, gases collected at the anode (at 100 mA cm^{-2}) were subjected to mass spectrometry (MS) and electrolytes were subjected to an o-tolidine indicator test because Cl_2 can react with OH^- in alkaline electrolyte and the produced ClO^- can be detected by the o-tolidine indicator test.[54] As shown in Fig. 5c, only O_2 and no Cl_2 is produced at the anode. No characteristic absorption peak was observed in the UV–vis spectra of the electrolytes from the Ru–BO_x–OH-300‖Ru–BO_x–OH-300 system after 200 hours of operation. In contrast, electrolytes remaining in the Ru–O_x-300‖Ru–O_x-300 and Pt/C‖RuO_2 systems are yellow and their absorption spectra contain peaks at *ca.* 437 nm (Fig. S30 and the detailed description, ESI†). These results indicate that electrolytic seawater splitting promoted by the

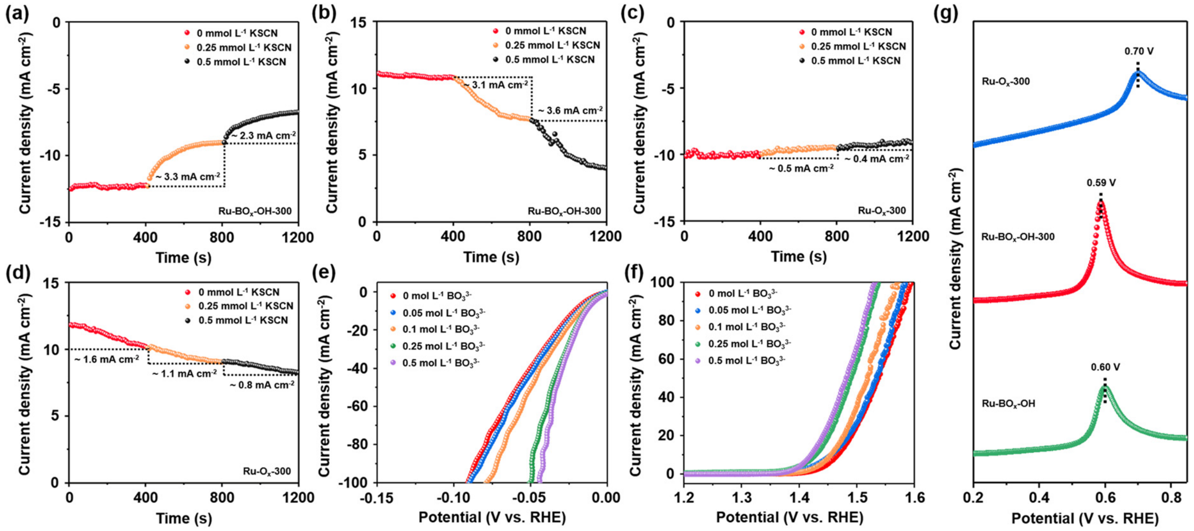

Fig. 4 Current density–time (*j*–*t*) curves of Ru–BO_x–OH-300 and Ru–O_x-300 in alkaline seawater with varying KSCN concentrations. (a) HER and (b) OER of Ru–BO_x–OH-300. (c) HER and (d) OER of Ru–O_x-300. (e) HER and (f) OER LSV curves of Ru–BO_x–OH-300 at different concentrations of BO_3^{3-} in alkaline seawater. (g) LSV curves of Ru–BO_x–OH, Ru–BO_x–OH-300 and Ru–O_x-300 in CO-saturated alkaline seawater electrolyte.

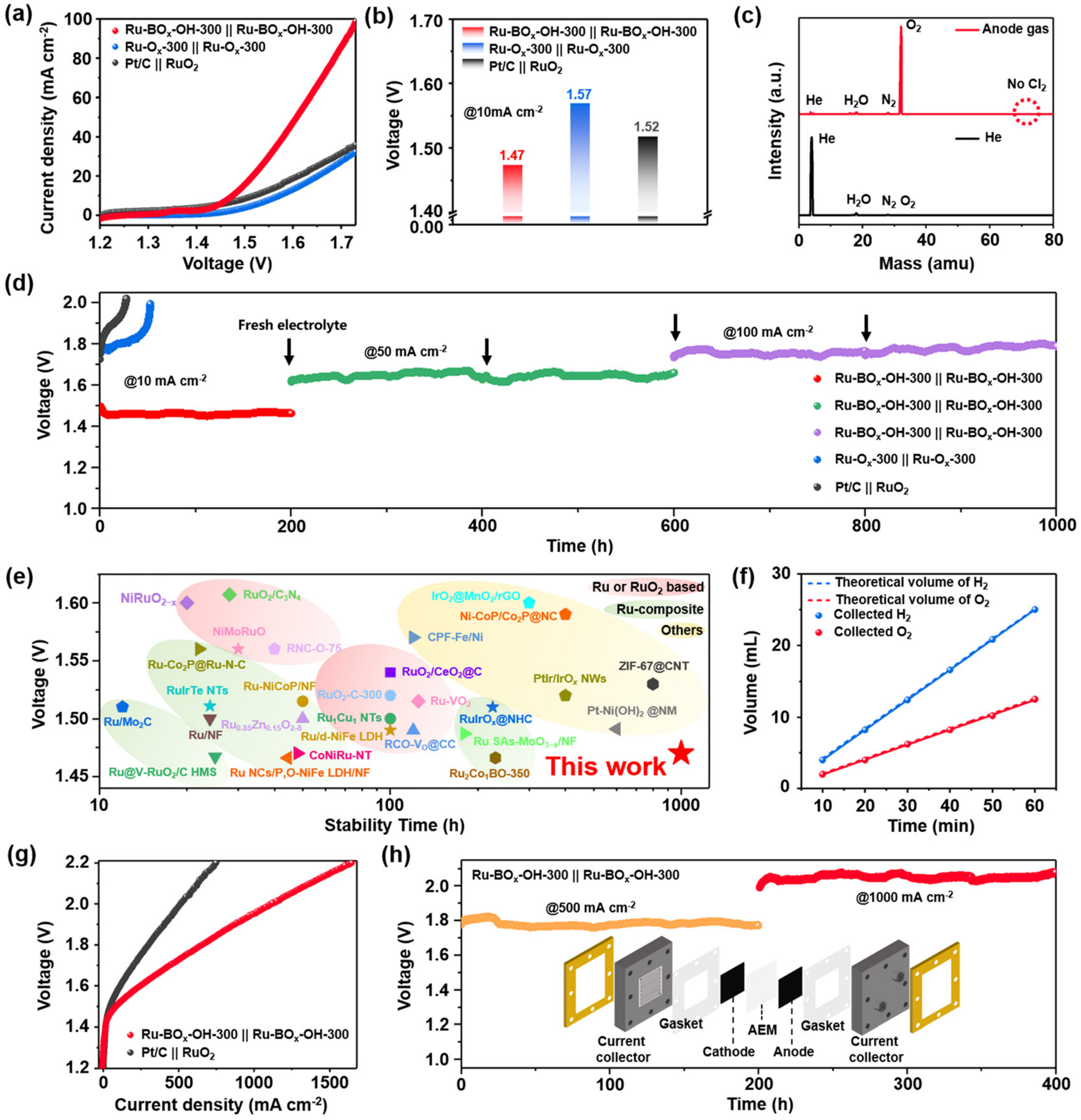

Fig. 5 Overall alkaline seawater splitting performance of Ru–BO$_x$–OH-300‖Ru–BO$_x$–OH-300, Ru–O$_x$-300‖Ru–O$_x$-300 and Pt/C‖RuO$_2$. (a) Polarization curves. (b) Comparison of voltage at 10 mA cm^{-2}. (c) Mass spectra of the anode gas and carrier gas (He). (d) Long-term stability at current densities of 10, 50 and 100 mA cm^{-2}. (e) Comparison of the voltage at 10 mA cm^{-2} and stability time between Ru–BO$_x$–OH-300 and other reported catalysts for water/seawater splitting in different media. (f) Volume of collected H$_2$ and O$_2$ gases for Ru–BO$_x$–OH-300 catalyst *versus* time and theoretical volume of gases. (g) Polarization curves of Ru–BO$_x$–OH-300‖Ru–BO$_x$–OH-300 and Pt/C‖RuO$_2$ in the AEMWE operated in a 1.0 M KOH + seawater electrolyte. (h) Stability test of Ru–BO$_x$–OH-300‖Ru–BO$_x$–OH-300 in the AEMWE at 500 and 1000 mA cm^{-2}; inset is a schematic diagram of an AEMWE.

Ru–BO$_x$–OH-300 electrode does not lead to Cl$_2$ or ClO$^-$ formation. Furthermore, Ru–BO$_x$–OH-300‖Ru–BO$_x$–OH-300 exhibits high electrocatalytic activity for at least 1000 hours at current densities of 10, 50 and 100 mA cm^{-2} (Fig. 5d), which was superior to those of Ru–O$_x$-300‖Ru–O$_x$-300 (inactivated after *ca.* 52 hours) and Pt/C‖RuO$_2$ (inactivated after *ca.* 27 hours). The Ru–BO$_x$–OH-300‖Ru–BO$_x$–OH-300 based device also shows excellent overall water splitting performance and durability in 0.5 mol L^{-1} H$_2$SO$_4$ and 1.0 mol L^{-1} KOH (see Fig. S31 and a detailed description, ESI†). The remarkable performance and stability of Ru–BO$_x$–OH-300 in the two-electrode system are comparable to those of other prominent electrocatalysts described recently (Fig. 5e, Table S8, ESI†). The Ru–BO$_x$–OH-300‖Ru–BO$_x$–OH-300 seawater splitting device was then paired with a commercial Si solar cell to assess faradaic efficiency (Fig. S32, ESI†). The evolution of H$_2$ and O$_2$ bubbles takes place simultaneously upon exposure to simulated solar irradiation. The faradaic efficiency was calculated to be *ca.* 97.6% (see Fig. 5f, S33, Table S9 and a detailed description, ESI†).

Finally, anion-exchange membrane water electrolyzers (AEMWEs) were assembled using Ru–BO$_x$–OH-300‖Ru–BO$_x$–OH-300 and Pt/C‖RuO$_2$ to further evaluate the practical application potential of the Ru–BO$_x$–OH-300 electrocatalyst in seawater electrolysis (Fig. S34, ESI†). The Ru–BO$_x$–OH-300‖Ru–BO$_x$–OH-300 electrolyzer exhibits improved seawater electrolysis performance compared with the Pt/C‖RuO$_2$ electrolyzer; to be specific, the Ru–BO_x–OH-300-based electrolyzer (at 25 °C) requires only 1.73 or 1.95 V to reach a current density of 500 or 1000 mA cm^{-2}, respectively (Fig. 5g). More importantly, the Ru–BO_x–OH-300‖Ru–BO_x–OH-300 electrolyzer exhibits excellent stability for 400 hours at current densities of 500 and 1000 mA cm^{-2} without obvious decay (Fig. 5h). The results suggest that the Ru–BO_x–OH-300 electrocatalyst is a highly promising option for practical use in overall seawater splitting.

DFT calculations

To gain further information about the nature of the improved OER performance and Cl^- corrosion resistance caused by the hydroxyl and borate species in Ru–BO_x–OH-300, density functional theory (DFT) calculations were conducted. The RuO_x–BO_x–OH surface was utilized as a model of Ru–BO_x–OH-300, and surfaces of the RuO_x–BO_x and RuO_2 were included to understand the effects of the hydroxyl and borate species (see Fig. S35 and a detailed description, ESI†). Considering that an abundance of H_2O molecules and OH^- exist in the OER in an alkaline electrolyte, DFT calculations were carried out on H_2O dissociation and the four-electron transfer pathway (Fig. S36, ESI†).[55] The energy barriers for H_2O dissociation from Ru centres in RuO_x–BO_x–OH, RuO_x–BO_x and RuO_2 were calculated to be 0.58, 0.75 and 0.91 eV (Fig. 6a), respectively, suggesting that the hydroxyl and borate species enhance H_2O dissociation, which contributes to OH* formation. The calculated Gibbs free energies of the four-electron transfer steps in the OER are shown in Fig. 6b. Notably, the OER performance is determined by the rate-determining step (RDS) in the RuO_x–BO_x–OH and RuO_x–BO_x conversions corresponding to the transformation from O* to OOH* (1.47 eV and 1.61 eV, respectively), while the RDS for the RuO_2 conversion is the transformation of OOH* to O_2 (2.05 eV). This result indicates the high intrinsic OER activity of RuO_x–BO_x–OH caused by the presence of the borate species that change the RDS of RuO_x–BO_x–OH in Ru sites and hydroxyl species decrease the reaction energy barrier.

Considering that the chloride evolution reaction is the main competing process taking place at the anode during seawater splitting, the Cl^- adsorption behavior on the RuO_x–BO_x–OH, RuO_x–BO_x and RuO_2 models was further assessed. Strong Cl^- absorption leads to poisoning of the catalytically active Ru sites and acceleration of the structural destruction of Ru in the catalysts.[56] Calculations on the RuO_x–BO_x–OH and RuO_x–BO_x models predict that they have higher Cl^- adsorption energies (−0.24 and −0.35 eV, respectively) than that of the RuO_2 model (−1.44 eV) (Fig. 6c). This finding suggests that RuO_x–BO_x–OH has the weakest interaction with Cl^-, which is beneficial for avoiding CER and Cl^- corrosion. Additionally, the partial density of states (PDOS) of the Ru 4d orbital further indicates that the d-band centers of RuO_x–BO_x–OH and RuO_x–BO_x (−1.31 and −1.33 eV, respectively) are more negative with respect to the Fermi level than that of RuO_2 (−1.13 eV), suggesting weaker adsorption of Cl^- on the surfaces of RuO_x–BO_x–OH and RuO_x–BO_x (Fig. 6d). Furthermore, the charge density distribution of the adsorption of Cl^- on Ru sites in RuO_x–BO_x–OH, RuO_x–BO_x and RuO_2 shows that the introduction of borate species causes the surfaces to have nonuniform charge distributions and electron redistribution (Fig. S37, ESI†). Thus, the calculations suggest that the borate species effectively optimize the electronic structure around the Ru sites and avoid Cl^- adsorption. The DFT calculations agree well with the experimental findings that hydroxyl and borate species improve the electrocatalytic activity for the OER, and borate species are responsible for weakening the adsorption of Cl^- and inhibiting the CER.

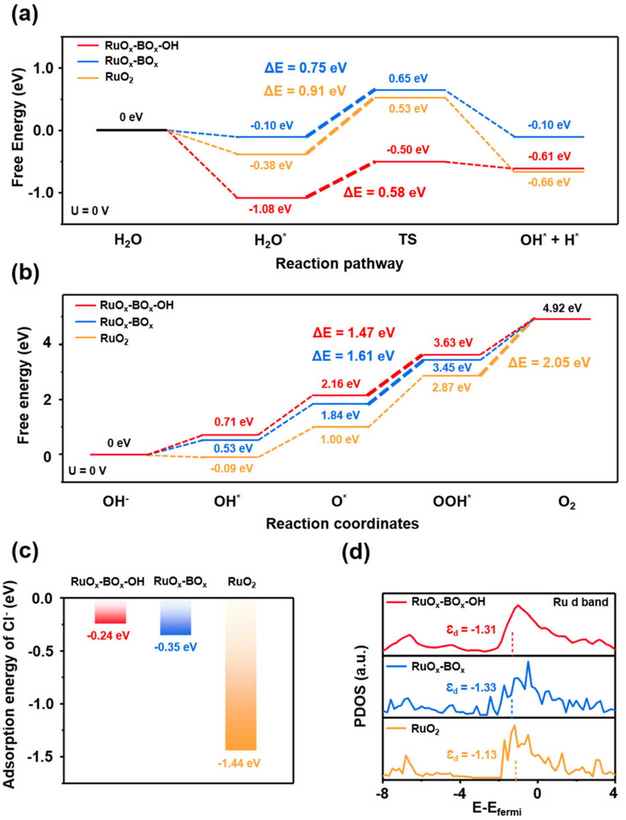

Fig. 6 (a) Dissociation of H_2O on Ru–BO_x–OH, RuO_x–BO_x and RuO_2. (b) Calculated free-energy diagrams for the $4e^-$ OER steps on Ru–BO_x–OH, RuO_x–BO_x and RuO_2. (c) Calculated free-energy diagrams of Cl^- adsorption on Ru–BO_x–OH, Ru–BO_x and RuO_2. (d) Calculated Ru d band in RuO_x–BO_x–OH, RuO_x–BO_x and RuO_2.

The remarkable electrocatalytic performance and stability of Ru–BO_x–OH-300 can thus be attributed to (1) the mild synthesis procedure to form the rich surface hydroxyl and borate species, (2) the hydroxyl and borate species that can increase the hydrophilicity and enhance the water adsorption to promote the water-involved reactions, and (3) the hydroxyl and borate species that can optimize the electronic structure of Ru for appropriate adsorption of intermediates in the OER; besides, the borate species are beneficial for weakening the adsorption of Cl^- and avoiding Cl^- corrosion.

Conclusions

In summary, we developed a facile wet chemical and low-temperature heat treatment method for efficiently introducing hydroxyl and borate species to create a durable Ru-based catalyst for alkaline seawater splitting. The hydroxyl and borate species improve the electrocatalytic properties of the Ru-based material by increasing hydrophilicity and regulating the electronic structure of the Ru sites. These alterations lead to an acceleration of the water splitting process and prevention of Cl^- corrosion. The newly prepared Ru–BO_x–OH-300 electrocatalyst displays outstanding bifunctional performance and durability for promoting both the HER and OER in alkaline seawater. The results of this study have a profound impact on understanding the inherent mechanism of water splitting catalyzed by Ru–BO_x–OH-T nanoparticles and provide a background for strategies to design new catalysts whose activities and stabilities can be regulated by introducing surface-reactive species.

Author contributions

L.-W. S., Y. W., L. S., Y. Liu, M.-X. H., W.-Y. Z. and K.-Y. X. performed synthesis and electrocatalytic performance studies. X.-Y. Y. conceived the project and provided the idea. L.-W. S. and Y. W. designed the experiments and analyzed the data. G.T. performed TEM and EDS characterization. J.-B. C. performed DFT calculations and data analysis. L.-W. S., Y. W., L. S., S.-M. W., Y. Lu, J. Y. and X.-Y. Y. wrote and revised the paper. M. M. T. and C. J. took part in discussions and revised the paper. All authors discussed the results, analyzed the data, and gave approval to the final version of the manuscript.

Conflicts of interest

There are no conflicts to declare.

Acknowledgements

This study was supported by the National Key Research and Development Program of China (2022YFB3805600, 2022YFB3805604), National Natural Science Foundation of China (22293020, 52201286), Major Program (JD) of Hubei Province (2023BAA003), China Postdoctoral Science Foundation (2023M732722), National 111 project (B20002), Guangdong Basic and Applied Basic Research Foundation (2022A1515010137, 2022A1515010504, 2022A1515-011905), Shenzhen Science and Technology Program (GJHZ202107-05143204014, JCYJ20210324142010029, KCXFZ20211020170006010), the Fundamental Research Funds for the Central Universities (WUT: 2023IVA095, WUT: 2023IV030h, WUT: 2023IVB086), a joint NSFC-DFG Project (NSFC grant 51861135313, DFG JA466/39-1), Jilin Province Science and Technology Development Plan (20220101248JC).

Notes and references

1 Y. Luo, Z. Zhang, M. Chhowalla and B. Liu, *Adv. Mater.*, 2022, **34**, 2108133.
2 L. Shen, J. Ying, K. I. Ozoemena, C. Janiak and X.-Y. Yang, *Adv. Funct. Mater.*, 2022, **32**, 2110851.
3 P. Farràs, P. Strasser and A. J. Cowan, *Joule*, 2021, **5**, 1921–1923.
4 J. N. Hausmann, R. Schlögl, P. W. Menezes and M. Driess, *Energy Environ. Sci.*, 2021, **14**, 3679–3685.
5 J. Huang, B. Hu, J. Meng, T. Meng, W. Liu, Y. Guan, L. Jin and X. Zhang, *Energy Environ. Sci.*, 2024, **17**, 1007–1045.
6 W. He, X. Li, C. Tang, S. Zhou, X. Lu, W. Li, X. Li, X. Zeng, P. Dong, Y. Zhang and Q. Zhang, *ACS Nano*, 2023, **17**, 22227–22239.
7 H. Fei, R. Liu, T. Liu, M. Ju, J. Lei, Z. Wang, S. Wang, Y. Zhang, W. Chen, Z. Wu, M. Ni and J. Wang, *Adv. Mater.*, 2023, 2309211.
8 H. Jin, J. Xu, H. Liu, H. Shen, H. Yu, M. Jaroniec, Y. Zheng and S.-Z. Qiao, *Sci. Adv.*, 2023, **9**, eadi7755.
9 C. He, Z. Liu, J. Wu, X. Pan, Z. Fang, J. Li and B. A. Bryan, *Nat. Commun.*, 2021, **12**, 4667.
10 J. Liu, S. Duan, H. Shi, T. Wang, X. Yang, Y. Huang, G. Wu and Q. Li, *Angew. Chem., Int. Ed.*, 2022, **61**, e202210753.
11 S.-T. Xiao, R. Yin, L. Wu, S.-M. Wu, G. Tian, M. Shalom, L.-Y. Wang, Y.-T. Wang, F.-F. Pu, H.-N. Barad, F. Wang and X.-Y. Yang, *Nano Lett.*, 2023, **23**, 4390–4398.
12 J. Ying, J.-B. Chen, Y.-X. Xiao, S. I. Cordoba de Torresi, K. I. Ozoemena and X.-Y. Yang, *J. Mater. Chem. A*, 2023, **11**, 1634–1650.
13 S. C. Sun, H. Jiang, Z. Y. Chen, Q. Chen, M. Y. Ma, L. Zhen, B. Song and C. Y. Xu, *Angew. Chem., Int. Ed.*, 2022, **61**, e202202519.
14 Y. L. Wu, X. Li, Y. S. Wei, Z. Fu, W. Wei, X. T. Wu, Q. L. Zhu and Q. Xu, *Adv. Mater.*, 2021, **33**, 2006965.
15 J. Jiao, N. N. Zhang, C. Zhang, N. Sun, Y. Pan, C. Chen, J. Li, M. Tan, R. Cui, Z. Shi, J. Zhang, H. Xiao and T. Lu, *Adv. Sci.*, 2022, **9**, 2200010.
16 Y. Liu, L. Chen, Y. Wang, Y. Dong, L. Zhou, S. I. Córdoba de Torresi, K. I. Ozoemena and X.-Y. Yang, *Front. Chem. Sci. Eng.*, 2023, **17**, 1698–1706.
17 Y. Wen, C. Liu, R. Huang, H. Zhang, X. Li, F. P. Garcia de Arquer, Z. Liu, Y. Li and B. Zhang, *Nat. Commun.*, 2022, **13**, 4871.
18 F. Fang, Y. Wang, L. W. Shen, G. Tian, D. Cahen, Y. X. Xiao, J. B. Chen, S. M. Wu, L. He, K. I. Ozoemena, M. D. Symes and X. Y. Yang, *Small*, 2022, **18**, 2203778.
19 J. Xie, F. Wang, Y. Zhou, Y. Dong, Y. Chai and B. Dong, *Nano-Micro Lett.*, 2023, **16**, 39.
20 L. Wu, M. J. Liao, B. Zhao, Q. N. Li, B. Liu and Y. X. Zhang, *Phys. Chem. Chem. Phys.*, 2023, **25**, 9264–9272.
21 L. Hui, Y. Xue, B. Huang, H. Yu, C. Zhang, D. Zhang, D. Jia, Y. Zhao, Y. Li, H. Liu and Y. Li, *Nat. Commun.*, 2018, **9**, 5309.
22 P. R. Chowdhury, H. Medhi, K. G. Bhattacharyya and C. M. Hussain, *Coord. Chem. Rev.*, 2024, **501**, 215547.
23 J.-B. Chen, J. Ying, Y.-X. Xiao, Y. Dong, K. I. Ozoemena, S. Lenaerts and X.-Y. Yang, *Sci. China Mater.*, 2022, **65**, 2685–2693.
24 K. L. Wu, L. X. Shi, Z. D. Wang, Y. Zhu, X. Y. Tong, W. X. He, J. W. Wang, L. R. Zheng, Y. S. Kang, W. L. Shan, Z. G. Wang, A. J. Huang and B. B. Jiang, *Chem. Commun.*, 2023, **59**, 3138–3141.

25 S. T. Xiao, S. M. Wu, L. Wu, Y. Dong, J. W. Liu, L. Y. Wang, X. Y. Chen, Y. T. Wang, G. Tian, G. G. Chang, M. Shalom, P. Fornasiero and X. Y. Yang, *ACS Nano*, 2023, **17**, 18217–18226.

26 S. Gligorovski, R. Strekowski, S. Barbati and D. Vione, *Chem. Rev.*, 2015, **115**, 13051–13092.

27 I. Danaee, O. Ghasemi, G. R. Rashed, M. Rashvand Avei and M. H. Maddahy, *J. Mol. Struct.*, 2013, **1035**, 247–259.

28 Y.-J. Zhang, S.-T. Xiao, Y.-T. Wang, F.-J. Wu, S.-M. Wu, L. Wu, F.-F. Pu, L.-Y. Wang, G. Tian, C.-Y. Huang and X.-Y. Yang, *New J. Chem.*, 2023, **47**, 17026–17031.

29 S.-T. Xiao, S.-M. Wu, Y. Dong, J.-W. Liu, L.-Y. Wang, L. Wu, Y.-X. Zhang, G. Tian, C. Janiak, M. Shalom, Y.-T. Wang, Y.-Z. Li, R.-K. Jia, D. W. Bahnemann and X.-Y. Yang, *Chem. Eng. J.*, 2020, **400**, 125909.

30 M. Chen, N. Kitiphatpiboon, C. Feng, Q. Zhao, A. Abudula, Y. Ma, K. Yan and G. Guan, *Appl. Catal., B*, 2023, **330**, 122577.

31 X. Zou, W. Zhang, X. Zhou, K. Song, X. Ge and W. Zheng, *J. Energy Chem.*, 2022, **72**, 509–515.

32 C. Liu, B. Sheng, Q. Zhou, D. Cao, H. Ding, S. Chen, P. Zhang, Y. Xia, X. Wu and L. Song, *Nano Res.*, 2022, **15**, 7008–7015.

33 S. Gupta, M. K. Patel, A. Miotello and N. Patel, *Adv. Funct. Mater.*, 2020, **30**, 1906481.

34 Y. Qiao, P. Yuan, C.-W. Pao, Y. Cheng, Z. Pu, Q. Xu, S. Mu and J. Zhang, *Nano Energy*, 2020, **75**, 104881.

35 P. R. Jothi, K. Yubuta and B. P. T. Fokwa, *Adv. Mater.*, 2018, **30**, 1704181.

36 J. M. V. Nsanzimana, L. Gong, R. Dangol, V. Reddu, V. Jose, B. Y. Xia, Q. Yan, J. M. Lee and X. Wang, *Adv. Energy Mater.*, 2019, **9**, 1901503.

37 L. Li, C. Tang, X. Cui, Y. Zheng, X. Wang, H. Xu, S. Zhang, T. Shao, K. Davey and S. Z. Qiao, *Angew. Chem., Int. Ed.*, 2021, **60**, 14131–14137.

38 Y. D. Yin, R. M. Rioux, C. K. Erdonmez, S. Hughes, G. A. Somorjai and A. P. Alivisatos, *Science*, 2004, **304**, 711–714.

39 M. Yu, C. Weidenthaler, Y. Wang, E. Budiyanto, E. Onur Sahin, M. Chen, S. DeBeer, O. Rudiger and H. Tuysuz, *Angew. Chem., Int. Ed.*, 2022, **61**, e202211543.

40 D. J. Morgan, *Surf. Interface Anal.*, 2015, **47**, 1072–1079.

41 J. Masa, I. Sinev, H. Mistry, E. Ventosa, M. de la Mata, J. Arbiol, M. Muhler, B. Roldan Cuenya and W. Schuhmann, *Adv. Energy Mater.*, 2017, **7**, 1700381.

42 S. Vinoth, H. T. Das, M. Govindasamy, S. F. Wang, N. S. Alkadhi and M. Ouladsmane, *J. Alloys Compd.*, 2021, **877**, 160192.

43 M. S. Maru, S. Ram, R. S. Shukla and N.-u H. Khan, *Mol. Catal.*, 2018, **446**, 23–30.

44 X. Chen, X.-T. Wang, J.-B. Le, S.-M. Li, X. Wang, Y.-J. Zhang, P. Radjenovic, Y. Zhao, Y.-H. Wang, X.-M. Lin, J.-C. Dong and J.-F. Li, *Nat. Commun.*, 2023, **14**, 5289.

45 J.-T. Ren, L. Chen, W.-W. Tian, X.-L. Song, Q.-H. Kong, H.-Y. Wang and Z.-Y. Yuan, *Small*, 2023, **19**, 2300194.

46 H. Y. Wang, L. Wang, J. T. Ren, W. Tian, M. Sun, Y. Feng and Z. Y. Yuan, *ACS Nano*, 2023, **17**, 10965–10975.

47 J.-T. Ren, L. Chen, H.-Y. Wang, W.-W. Tian, X. Zhang, T.-Y. Ma, Z. Zhou and Z.-Y. Yuan, *Appl. Catal., B*, 2023, **327**, 122466.

48 H.-Y. Wang, J.-T. Ren, L. Wang, M.-L. Sun, H.-M. Yang, X.-W. Lv and Z.-Y. Yuan, *J. Energy Chem.*, 2022, **75**, 66–73.

49 L. Deng, S.-F. Hung, S. Zhao, W.-J. Zeng, Z.-Y. Lin, F. Hu, Y. Xie, L. Yin, L. Li and S. Peng, *Energy Environ. Sci.*, 2023, **16**, 5220.

50 S. Li, Z. Li, R. Ma, C. Gao, L. Liu, L. Hu, J. Zhu, T. Sun, Y. Tang, D. Liu and J. Wang, *Angew. Chem., Int. Ed.*, 2021, **60**, 3773–3780.

51 P. Han, X. Yang, L. Wu, H. Jia, J. Chen, W. Shi, G. Cheng and W. Luo, *Adv. Mater.*, 2024, **36**, 2304496.

52 J. Zhang, L. Zhang, J. Liu, C. Zhong, Y. Tu, P. Li, L. Du, S. Chen and Z. Cui, *Nat. Commun.*, 2022, **13**, 5497.

53 Y. Duan, Z. Yu, L. Yang, L. Zheng, C. Zhang, X. Yang, F. Gao, X. Zhang, X. Yu, R. Liu, H. Ding, C. Gu, X. Zheng, L. Shi, J. Jiang, J. Zhu, M. Gao and S. Yu, *Nat. Commun.*, 2020, **11**, 4789.

54 J. Li, Y. Liu, H. Chen, Z. Zhang and X. Zou, *Adv. Funct. Mater.*, 2021, **31**, 2101820.

55 J.-B. Chen, J. Ying, Y.-X. Xiao, G. Tian, Y. Dong, L. Shen, S. I. Córdoba de Torresi, M. D. Symes, C. Janiak and X.-Y. Yang, *ACS Catal.*, 2023, **13**, 14802–14812.

56 X. Liu, J. Chi, H. Mao and L. Wang, *Adv. Energy Mater.*, 2023, **13**, 2301438.